Atmos. Meas. Tech. Discuss., 6, 10653–10698, 2013
www.atmos-meas-tech-discuss.net/6/10653/2013/
doi:10.5194/amtd-6-10653-2013

Atmospheric Measurement Techniques Discussions

The mobile Water vapor Aerosol Raman LIdar and its implication in the frame of the HyMeX and ChArMEx programs: application to a dust transport process

P. Chazette, F. Marnas, and J. Totems

Laboratoire des Sciences du Climat et de l'Environnement (LSCE), UMR8212, Laboratoire mixte CEA-CNRS-UVSQ, CEA Saclay, 91191 Gif-sur-Yvette, France

Received: 3 November 2013 – Accepted: 29 November 2013 – Published: 10 December 2013

Correspondence to: P. Chazette (patrick.chazette@lsce.ipsl.fr)

Published by Copernicus Publications on behalf of the European Geosciences Union.

Abstract

The increasing importance of the coupling of water and aerosol cycles in environmental applications requires observation tools which allow simultaneous measurements of these two fundamental processes for climatological and meteorological studies. In this purpose, a new mobile Raman lidar, WALI (Water vapor and Aerosol LIDAR), has been developed and implemented within the framework of the international HyMeX/IODA-MED and ChArMEx programs. This paper presents the key properties of this new device and its first applications to scientific studies. The lidar uses an eye-safe emission in the ultra-violet range at 354.7 and a set of compact refractive receptors. Cross-comparisons between rawindsoundings performed from balloon or aircraft and lidar measurements have shown a good agreement in the derived water vapor mixing ratio (WVMR). The discrepancies are generally less than 0.5 g kg^{-1} and therefore within the error bars of the instruments. A detailed study of the uncertainties was conducted and shows a 7 to 11 % accuracy of the WVMR retrieval, which is largely constrained by the quality of the calibration. It also proves that the lidar is able to measure the WVMR during ~~the day~~ over a range of about 1 km. The WALI system otherwise provides measurements of aerosol optical properties such as the lidar ratio (~~LR~~) or the particulate depolarization ratio (PDR). An important example of scientific application addressing the main objectives of the HyMeX and ChArMEx programs is then presented, following an event of desert dust aerosols over the Balearic Islands. This dust intrusion may have had a significant impact on the intense precipitations that occurred over south-western France and the Spanish Mediterranean coasts. During this event, the LR and PDR values obtained are in the ranges of $\sim$ 45–63 $\pm$ 6 sr and 0.1–0.19 $\pm$ 0.01, respectively, which is representative of dust aerosols. The dust layers are also shown to be associated with significant WVMR, i.e. between 4 and 6.7 g kg^{-1}.

AMTD
6, 10653–10698, 2013

1 Introduction

By the end of the 21st century, climate models forecast a significant increase in the loss of fresh water in densely populated areas. For instance, the decrease of fresh water reserves around the Mediterranean Sea has been assessed to be 40 % higher for 2070–2090 than for 1950–1999 (Sanchez-Gomez et al., 2009). These results should be evaluated in the context of rising anthropogenic pressure in the Mediterranean region, with a population growth expected in the range of 300 % around the Mediterranean basin within the next 25 yr (with more than 500 million inhabitants). The Mediterranean area has thus been identified as a hot-spot in the projection of future climate change (Giorgi and Lionello, 2008) where the water-vapor mixing ratio is a key meteorological parameter for the energy balance of the atmosphere (e.g. Melfi et al., 1989; Kulmala et al., 1993).

Moreover, it is now known that the cycles of aerosols, clouds and water-vapor are closely coupled within the climate change scenarios. Indeed, water-vapor is involved in the aerosol and cloud formation when aerosols contain hygroscopic components (e.g. Larson and Taylor, 1983; Rood et al., 1987; Radriamiarisoa et al., 2006) and thus influences the Earth-Atmosphere radiative balance. Aerosol hydration remains one of the largest sources of uncertain the climate models (Covert et al., 1979; Boucher and Anderson, 1995; Haywood et al., 1997). Aerosols also lead to a visibility reduction in the atmosphere, which impacts the socio-economical activities. As the densely populated areas of the planet are especially characterized by their vulnerability to changes in the coupled cycles of water and aerosol, precise measurements are now necessary to assess the model uncertainties in both the water-vapor mixing ratio and the aerosol amounts in the lo and middle troposphere.

Few instruments are available to simultaneously measure these two meteorological and climatic variables with a dense vertical sampling. As written by Whiteman et al. (1992), lidar is a well-established technique for measuring the water-vapor mixing ratio in the atmosphere. Cooney (1970) and Melfi et al. (1969) showed as early

AMTD
6, 10653–10698, 2013

as the late 1960's that the Raman lidar is a powerful tool for this measurement and Vaughan et al. (1988) used for the first time Raman lidar to perform water-vapor mixing ratio measurements up to the tropopause. Following these pioneer works, Ansmann et al. (1992) performed simultaneously measurement of the water-vapor mixing ratio and aerosol optical properties, Turner et al. (1999) used Raman lidar in continuous measurements in the framework of the atmospheric radiation measurement program (ARM), and Veselovskii et al. (2000) also yielded profiles of the water-vapor mixing ratio in the troposphere. The differential absorption lidar technique (e.g. Noah et al., 1994; Bruneau et al., 2001) could also be used but requires greater instrumental constraints and makes it difficult to comply with eye-safety conditions. Lidar is also an often-used instrument for aerosol survey (Fiocco and Grams, 1964) and particularly Raman lidar (e.g. Ansmann et al., 1992; Turner et al., 1999). More recently, an eye-safe, compact and light Nitrogen–Raman lidar has been developed at the Laboratoire des Sciences du Climat et de l'Environnement (LSCE) to track the aerosol pollution around Paris as well as the ash emitted in the atmosphere by the Eyjafjallajökull volcano (Royer et al., 2010; Chazette et al., 2011). The natural evolution of such a lidar, in the frame of the scientific programs Hydrological cycle in the Mediterranean eXperiment (HyMeX, http://www.hymex.org/) and Chemistry-Aerosol Mediterranean Experiment (ChArMEx, http://www.mistrals-home.org), was the addition of a water-vapor Raman channel.

We present in this paper the new transportable eye-safe and mobile Water-vapor and Aerosol Raman LIdar (WALI) that is able to measure simultaneously the water-vapor mixing ratio (WVMR) and the aerosol optical properties with a sufficient stability for meteorological and climatological studies in the lower and middle troposphere. The first results obtained on the retrieval of the WVMR and aerosol optical properties will be presented and discussed hereafter following the fall campaign of the HyMeX/IODA-MED (Innovative Observing and Data Assimilation systems for the MEDiterranean Weather) program. The datasets gathered on aerosol properties also represents the first measurements provided to the ChArMEx program.

AMTD
6, 10653–10698, 2013

In a first section, the Raman lidar will be presented along with the experimental set-up. The classical theoretical approaches for the retrieval of the WVMR and aerosol optical properties will be also reminded. For the lidar calibration, a comparison to WVMR vertical soundings performed by rawindsoundings and aircraft measurements will be presented in a second section. The main uncertainties will be assessed and discussed in a third section. In a fourth section we will analyze an example of dust event observed in the frame of the HyMeX/IODA-MED and ChArMEx programs. Finally, the ~~conclusion~~ will recall the main characteristics of the instrument and the first results obtained.

2 Experimental and theoretical tools

The WALI instrument is here described as well as the signal processing used for the retrieval of both the WVMR and the aerosol optical properties. The experimental sites where lidar measurements have been performed are also presented.

2.1 Technical characteristics of WALI

The WALI instrument has been developed at LSCE based on the same technology than its precursor instruments LESAA (Lidar pour l'Etude et le Suivi de l'Aérosol Atmosphérique, (Chazette et al., 2005)) and LAUVA (Lidar Aérosol UltraViolet Aéroporté (Chazette et al., 2007; Raut and Chazette, 2009)). It is a home-made instrument mainly dedicated to atmospheric research activities.

The lidar operates with an emitted wavelength of 354.7 nm and is designed to fulfill eye-safe ~~conditions~~. Its emitter is a pulsed Nd:YAG laser (BRILLANT) manufactured by the QUANTEL company (www.quantel.com). The acquisition system is based on a PXI (PCI eXtensions for Instrumentation) technology with 12 bits digitizers at 200 MS s^{-1} (Mega sampling by second) manufactured by the National Instruments company. Its main characteristics are summarized in Table 1. During ~~all~~ the experiment the acquisition was performed for mean profiles of 1000 laser shots leading to a temporal sampling

AMTD
6, 10653–10698, 2013

close to 1 min. The UV pulse energy is ∼ 60 mJ and the pulse repetition frequency is 20 Hz.

A schematic presentation of WALI is given in Fig. 1. The receiver is composed of 3 distinct detection boards using small collector diameters of 15 cm. The total number of detection channels is four. Using short focal length refractive telescopes instead of a reflector ensures a low altitude overlap for the lidar and increases its stability, transmittance and compactness. The wide field-of-view (FOV) ∼ 2.3 mrad allows a full-overlap of the transmission and reception paths beyond ∼ 200–300 m. On each channel optical detection is performed by a photomultiplier tube placed behind an ~~interferential~~ filter and a focusing lens. The amplification gain of the tube between its anode and cathode is directly linked to the input high voltage (HV) chosen by the lidar acquisition software. HV variation allows optimizing the detection dynamic for both nighttime and daytime measurements (with strong sky background light). It however requires a careful calibration of gain vs. HV when dealing with ratios of signals output from multiple channels. Note that the reason to have separate paths for the two Raman channels is to be able to set-up independently each channel to keep as much flexibility as possible.

The first board is dedicated to the detection of the elastic molecular, aerosols and cloud backscatter from the atmosphere. Two different channels are implemented on that board to detect (i) the total (co-polarized and cross polarized with respect to the laser emission) and (ii) the cross-polarized backscatter coefficients of the atmosphere. The separation between the two beams is carried out using a beam-splitter and a Brewster plate. The interferential filters (IF1), with spectral bandwidths of 0.2 nm, are manufactured by Barr Associates. This reception channel design is similar to the one used for previous studies on tropospheric aerosols (e.g. Royer et al., 2011; Chazette et al., 2012). The second and third boards are dedicated to the measurements of the inelastic nitrogen (N_2-channel) and water vapor (H_2O-channel) Raman backscattered signals. They measure the backscattered Stokes component of the inelastic vibrational Raman scattering because this process is much more likely at the typical tropospheric temperatures (compared to the anti-Stokes component of Raman scattering). Such scattering

AMTD
6, 10653–10698, 2013

happens at a larger wavelength than that emitted, i.e. ∼ 386.6 nm and ∼ 407.5 nm for N_2- and H_2O-channel, respectively. The measured water-vapor Raman signal is ∼ 4 orders of magnitude (∼ 3 orders for the nitrogen Raman signal) less than the elastic backscattered signal. Therefore, the H_2O-channel was found to require an extremely high rejection of all radiation apart from the Raman Stokes central peak, with a transmission ratio approaching 10 orders of magnitude, assuming a complete rejection of the elastic Rayleigh–Mie return (Whiteman et al., 1992, 2007). This is done by using a dichroic plate, as drawn in Fig. 1, associated to a specific interference filter. The spectral bandwidth of this interference filter (IF3), also built by Barr Associates, is 0.3 nm to optimize the contribution of the rotational lines considering the signal to noise ratio. The N_2-channel is equipped with both a Brewster plate to decrease the background sky contribution and a Barr Associate interferential filter (IF2) with a 0.2 nm spectral bandwidth. Note that, considering the spectral bandwidths of the interference filters used here, the Raman backscatter cross sections do not depend on the atmospheric temperature (Bribes et al., 1976; Penney and Lapp, 1976; Whiteman et al., 1992).

2.2 Lidar signal parameterization

The range corrected lidar signals S_λ at wavelength λ of a ground-based lidar situated at the altitude z_G above the mean sea level (a.m.s.l.) is given as a function of backscatter coefficient β_j, and aerosol (molecular) extinction coefficient $\alpha_{a(m)}$ against altitude z by (e.g. Measures, 1984)

$$S_\lambda(z) = C_\lambda \cdot F_\lambda(z) \cdot \beta_\lambda(z) \cdot \exp\left(-\int_{z_G}^{z} \left[(1 + \eta_{m\lambda}) \cdot \alpha_m(z') + (1 + \eta_{a\lambda}(z)) \cdot \alpha_a(z') \right] \cdot dz' \right) \quad (1)$$

Where: (i) for the elastic channel at $\lambda = 354.67$ nm (subscript E thereafter), $\beta_E(z) = k_f \frac{3\alpha_m(z)}{8\pi} + \frac{\alpha_a(z)}{LR(z)}$, is the sum of the molecular (m, $\beta_m(z) = k_f \frac{3\alpha_m(z)}{8\pi}$) and the aerosol~~ar~~ (a, $\beta_a(z) = \frac{\alpha_a(z)}{LR(z)}$), with k_f the King factor of air (King, 1923) and LR the lidar ratio, (ii) for the

AMTD
6, 10653–10698, 2013

nitrogen Raman channel at $\lambda = 386.63$ nm (subscript N thereafter), $\beta_N(z) = N_N(z) \cdot \sigma_N^\pi$, with the nitrogen density profile $N_N(z)$, and (iii) for the water-vapor Raman channel at $\lambda = 407.5$ nm (subscript H thereafter), $\beta_H(z) = N_H(z) \cdot \sigma_H^\pi$, with the water vapor density profile $N_H(z)$. σ_x^π stands for the Raman differential backscatter cross section of the nitrogen (x = N) or water-vapor (x = H) channels. ~~Coefficients~~ $\eta_{m\lambda} = \left(\frac{\lambda}{354.67}\right)^{-4.09}$ and $\eta_{a\lambda}(z) = \left(\frac{\lambda}{354.67}\right)^{-A(z)}$ are used to take into account the spectral dependency effects due to the molecules and aerosols (via the Angstrom exponent A), respectively. Note that only zenithal lidar measurements have been performed during this work. C_λ are the instrumental constants. F_λ are the overlap functions, which have been experimentally measured during the campaign for each channel and shown on Fig. 2. The overlap function of the H_2O-channel has been deduced from both that of the N_2-channel and the calibration in terms of WVMR hereafter presented. It is not ~~total~~ under ~ 0.7 km because the field diaphragm did not collect the entire image field in the optical configuration used. Hence, a correction, which is included in the calibration process, has to be applied.

The molecular extinction and backscatter coefficients are determined with the polynomial approximation proposed by Nicolet (1984) using a reference atmospheric density calculated from ancillary measurements (e.g. Chazette et al., 2012). The uncertainty on the a priori knowledge of the molecular contribution has been previously assessed to be lower than 2 % (Chazette et al., 2010). Considering $k_f = 1$ leads to an overestimation on the molecular volume backscatter coefficient of only 1.5 % at 355 nm (Collis and Russel, 1976).

2.2.1 Water-vapor mixing ratio

The WVMR (r_H) is defined as the mass of water vapor divided by the mass of dry air in the same volume:

$$r_H(z) = \frac{N_H(z)}{N_N(z)} \cdot \frac{M_H}{M_N} \cdot r_N \quad (2)$$

AMTD
6, 10653–10698, 2013

where r_N is the nitrogen mixing ratio that can be considered as a constant in the troposphere. M_H and M_N are the molar masses of water-vapor and nitrogen, respectively. The WVMR can be directly derived from the ratio of the H_2O-channel and N_2-channel as

$$r_H(z) = K \cdot \xi(z) \cdot \frac{S_H(z)}{S_N(z)} \cdot \exp\left(-[\eta_{mN} - \eta_{mH}] \cdot \int_{z_G}^{z} \alpha_m(z') \cdot dz' - \int_{z_G}^{z} [\eta_{aN}(z') - \eta_{aH}(z')] \cdot \alpha_a(z') \cdot dz' \right) \quad (3)$$

where K is the instrumental constant, expressed as

$$K = \frac{C_N}{C_H} \cdot \frac{\sigma_N^{\pi}}{\sigma_H^{\pi}} \cdot \frac{M_H}{M_N} \cdot r_N \quad (4)$$

ξ is the ratio between the overlap factors of the N_2-Raman and H_2O-Raman channels gradually approaching unity with altitude and reaching it around 700 m. Both K and ξ have to be assessed during a calibration procedure. In the second part of the equation, the second term represents the atmospheric corrections associated to the spectral dependencies of the extinction properties of both molecules and aerosols.

2.2.2 Aerosol optical properties

The retrieval of the aerosol optical properties coupled to backtrajectory analyses can contribute to the identification of the air mass origin and to the radiative balance studies above the Mediterranean basin. Those properties are obtained using the following procedure. Firstly, after the correction of the molecular contribution, the aerosol optical thickness (AOT) between a reference altitude z_0 and z is derived from the N_2-Channel by (e.g. Royer et al., 2011)

AMTD
6, 10653–10698, 2013

$$\mathrm{AOT}\,(z_0,z) = \frac{1}{(1+\eta_{\mathrm{aN}})}\cdot\left|\ln\left(\frac{S_{\mathrm{N}}(z_0)}{S_{\mathrm{N}}(z)}\cdot\frac{\beta_{\mathrm{N}}(z)}{\beta_{\mathrm{N}}(z_0)}\cdot\exp\left((1+\eta_{\mathrm{mN}})\int_{z_0}^{z}\alpha_{\mathrm{m}}(z')\cdot\mathrm{d}z'\right)\right)\right| \quad (5)$$

The reference altitude z_0 can be taken in the upper or lower parts of the lidar profile. Hence, the aerosol backscatter coefficient β_{a} can be directly calculated as

$$\beta_{\mathrm{a}}(z) = \beta_{\mathrm{E}}(z_0)\frac{S_{\mathrm{E}}(z)}{S_{\mathrm{E}}(z_0)} \cdot\exp\left(2\cdot\left[\mathrm{sgn}(z-z_0)\cdot\mathrm{AOT}\,(z_0,z)+\int_{z_0}^{z}\alpha_{\mathrm{m}}(z')\cdot\mathrm{d}z'\right]\right)-\beta_{\mathrm{m}}(z) \quad (6)$$

Secondly, the AOT can be used in two ways. The first one is via a regularization approach such as the Tikhonov regularization method (Tikhonov and Arsenin, 1977), from which the vertical profiles of LR and α_{a} are derived (e.g. Royer et al., 2011) starting from the matrix form of:

$$\mathrm{AOT}\,(z_0,z) = \left|\int_{z_0}^{z}\mathrm{LR}(z')\cdot\beta_{\mathrm{a}}(z')\cdot\mathrm{d}z'\right| \quad (7)$$

The second one is via an iterative algorithm using the Klett (1985) approach (Chazette, 2003; Royer et al., 2011):

$$\alpha_{\mathrm{a}}(z) = \overline{\mathrm{LR}}\cdot\left(\frac{S_{\mathrm{E}}(z)Q(z)}{\frac{S_{\mathrm{E}}(z_0)}{(\beta_{\mathrm{m}}(z_0)+\beta_{\mathrm{a}}(z_0))}+2\cdot\overline{\mathrm{LR}}\cdot\int_{z}^{z_0}S_{\mathrm{E}}(z')Q(z')\mathrm{d}z'}-\beta_{\mathrm{m}}(z)\right) \quad (8)$$

AMTD
6, 10653–10698, 2013

where Q is the correction related to the differential molecular optical thickness calculated from the vertical profile of the molecular scattering coefficient:

$$Q(z) = \exp\left(2\left[k_f \frac{3\cdot\overline{\mathrm{LR}}}{8\pi} - 1\right]\int_z^{z_0} \alpha_m(z')\mathrm{d}z'\right) \quad (9)$$

The columnar mean lidar ratio $\overline{\mathrm{LR}}$ that is derived from this second way corresponds to the value of LR(z) weighted by the aerosol extinction coefficient profile between z and z_0.

The depolarization of the laser beam by aerosols is also a powerful tracer to contribute to the identification of the airmass origins. Taking into account that the channel transmissions are not pure in terms of polarization, the volume depolarization ratio (VDR) is explained as (e.g. Chazette et al., 2012a)

$$\mathrm{VDR}(z) \approx \frac{T_1^{//}\cdot S_{E2}(z)}{R_c\cdot S_{E1}(z)} - \left(1-T_1^{//}\right)\cdot\left(1-T_2^{//}\right) \quad (10)$$

$T_1^{//}$ and $T_2^{//}$ are the parallel transmissions of the total and cross-polarization channels. They were estimated before and after the experiment in laboratory on a specific optical bench (Chazette et al., 2012a). The cross-calibration coefficient R_c can be assessed by normalizing the lidar signals obtained in a "clean" atmospheric volume with negligible aerosol content:

$$R_c \approx \frac{S_{E2}(z)\cdot T_1^{//}}{S_{E1}(z)\left[\left(1-T_1^{//}\right)\cdot\left(1-T_2^{//}\right)+\mathrm{VDR}_m\right]} \quad (11)$$

where the molecular volume depolarization ratio (VDR_m) was taken equal to 0.3945 % at 355 nm following Collis and Russel (1976). Therefore the particulate depolarization

AMTD
6, 10653–10698, 2013

ratio (PDR) is computed from

$$\mathrm{PDR}(z) = \frac{\beta_m(z)\cdot(\mathrm{VDR_m} - \mathrm{VDR}(z)) - \beta_a(z)\cdot\mathrm{VDR}(z)\cdot(1+\mathrm{VDR_m})}{\beta_m(z)\cdot(\mathrm{VDR}(z) - \mathrm{VDR_m}) - \beta_a(z)\cdot(1+\mathrm{VDR_m})} \quad (12)$$

2.3 Experimental sites

To ensure its mobility, WALI was embedded onboard the Mobile Aerosol Station van (Chazette et al., 2005) also equipped with a VAISALA 200 probe mounted on a mast at ∼ 10 m from the surface. Different experimental sites have been considered to calibrate and test WALI under field conditions. The first one is close to the Paris area at ∼ 30 km South of Paris (48°42′50″ N and 2°14′44″ E). It is situated east of the Trappes meteorological station where rawindsoundings are performed twice daily. The second one is close to Montpellier (43°37′14″ N and 4°4′11″ E) in the South of France close to the Mediterranean coast. This site has been selected for the opportunity of launching a simultaneous rawindsounding with the lidar measurements without problem for the air traffic. The third site is the one selected to conduct the HyMeX/IODA-MED fall campaign in 2012 and the ChArMEx summer campaign in 2013. Shown in Fig. 3, it is situated on the Balearic island of Menorca (Spain) to catch the water vapor amount before the airmasses reach the Spain and French coasts. The lidar-van was operated from a site close to Ciutadella (western part of the Menorca island, 39°60′00″ N and 3°50′20″ E) for HyMeX and close to Mahon (eastern part of the Menorca island, 39°49′32″ N and 4°12′30″ E) for ChArMEx. Rawindsounding were performed from Palma de Majorca (Majorca Island) at ∼ 100 km southwest from the lidar location. A dedicated calibration flight was also performed over Mahon in the eastern part of the Menorca Island, at about 40 km east of Ciutadella. The main experimental period took place between 10 September and 30 October 2012.

AMTD
6, 10653–10698, 2013

3 ~~Calibration~~ to retrieve the WVMR

As previously discussed, the vertical profile of the WVMR is retrieved using the ratio between the H_2O-Raman and N_2-Raman return signals. Nevertheless, this retrieval is subject to the prior assessment of both the calibration constant K and the overlap factor ratio ξ. Because of the uncertainties on the Raman backscatter cross-section and the difficulty to exactly characterize the optical transmission of the entire lidar detection system, the calibration has been performed comparatively to simultaneous vertical sounding using a well-qualified meteorological probe. Note that Vaughan et al. (1988) used a calibration on optical bench of each optical element leading to a final precision of 12 % on the WVMR.

For the same purpose, atmospheric water vapor profiles have been monitored in the Paris area, in the Southeast of France, and at Menorca before, during and after the HyMeX/IODA-MED campaign of the September–October 2012 (www.hymex.org). The calibration procedure has been conducted followings 3 chronological steps. (1) Lidar-derived WVMR profiles have been compared with specific nighttime rawindsoundings carried out by Meteo-France on 1 September and 27 October 2012 close to Paris and Montpellier, respectively. Hence, both K and ξ have been assessed. (2) Due to the difference of photomultipliers high voltage (HV) used during nighttime (950 and 1000 V for the N_2- and H_2O-channels, respectively) and daytime, a specific calibration function has been derived to allow continuity between the lidar measurements performed during night- and daytime, as K evolved against HV. (3) Independent rawindsoundings have been used to validate the previous calibrations using day- and night-time measurements performed from air-borne platforms equipped with VAISALA probes. These checks have been made before, during and after the campaign. Note that the WALI final vertical resolution has been fixed to 50 m for this calibration exercise.

Calibration. The rawindsounding performed near Montpellier was close to the lidar-van (~ 100 m), and is thus considered the most relevant mean to calibrate the lidar. It has been performed on 30 October 2012 during nighttime at 22:00 local time (LT).

AMTD
6, 10653–10698, 2013

The result after calibration with $K = 0.066$ is given in Fig. 4. The presence of clouds prevents us from verifying the agreement between the instruments over 1.6 km a.m.s.l.. The standard deviation (std) between the lidar- and rawindsounding-derived WVMR is 0.13 g kg^{-1} (~ 2.3 %). On the same figure, the rawindsounding station of Trappes has also been used to test the calibration with the same value $K = 0.066$ for a measurement performed in the Paris area (Palaiseau). The agreement is very good under 2 km a.m.s.l. with a std of 0.2 g kg^{-1} as the lidar-van was downwind from the station. Over 2 km the discrepancy increases with a std close to 0.5 g kg^{-1}. The presence of mid-altitude clouds can explain the difference between lidar and rawindsounding above 2.5 km a.m.s.l..

High voltage variation during daytime. The diurnal evolution of the calibration coefficient K has been measured by two specific experiments over Menorca during the fall of 2012. The result is shown Fig. 5 against the HVs of the N_2- and H_2O-Raman channels. During daytime the HVs were close to 850 and 650 V for the N_2- and H_2O-Raman channels, respectively. With such values K significantly increases to reach ~ 1. This calibration has been tested by measuring in the same airmass for HVs from 650 to 1000 V. Moreover, two areas (Menorca and Paris) with different WVMR have been considered as shown in Fig. 6. The results are in good agreement with a std between 0.2 and 1 km a.m.s.l. of ~ 0.8 and ~ 0.5 g kg^{-1} for Menorca and Paris, respectively. Note that the use of lower HVs leads to a decrease in the accessible altitude range because a lower PMT gain, chosen to avoid saturation by sky background light, decreases the signal to noise ratio.

Validation using independent rawindsoundings. The validation of the previous calibration has been carried out using measurements from balloon and aircraft. Figure 7 gives comparisons between WVMR retrieved from lidar and rawindsounding over the same previous sites of the Paris area, before, and several months after the IODA-MED campaign. The first (second) one is during nighttime (daytime). On 5 September 2012 the lidar and rawindsounding comparison leads to a std of 0.83 g kg^{-1} for WVMR between 0.3 and 5 km a.m.s.l.. The stronger discrepancy is mainly due to the

AMTD
6, 10653–10698, 2013

airmass variability in the lower part of the profile. The agreement is significantly better on 19 February 2013, with measurements performed during daytime. The std is equal to 0.29 g kg^{-1} between ~ 0.5 and 1.2 km.

A specific flight was performed above Mahon on 27 October 2012 between 08:30 and 09:30 LT. The meteorological probe used on the plane was a VAISALA PTB110-Veriteq SP2000. It delivers the thermodynamic temperature with an uncertainty of 0.15 K, the pressure with an uncertainty of 0.6 hPa and the relative humidity with a relative uncertainty of 5 % for the atmospheric conditions encountered in the low and middle troposphere. This leads to an absolute uncertainty of 0.67 g kg^{-1} on the WVMR. As shown in Fig. 8, when compared to the lidar-derived WVMR, the std is 0.55 g kg^{-1} for altitudes between 0.2 and 1.2 km a.m.s.l., which is close to the error bars. Note that for the lidar, the std is also due to the atmospheric fluctuations during a diurnal average of one hour. Nighttime comparison with the rawindsounding of Palma de Majorca leads to a similar std of 0.48 g kg^{-1}. Figure 8 also includes comparison to operational modeling. The first output is from ECMWF (European Center for Medium-Range Weather Forecasts, www.ecmwf.int) analyses. The 9 closest grid points from Ciutadella have been considered, showing that the WVMR below 2 km is not fluctuating much with a std of 0.22 g kg^{-1}. The second model is AROME WMED whose WVMR forecast has been extracted above the ground-based lidar location. It is a mesoscale model based on a three dimensional variational data assimilation system with a horizontal resolution of 2.5 km, centered over the western part of the Mediterranean basin for real-time and case-study uses. It has been developed for the preparation of the experimental HyMeX special observation period. It is derived from the operational version of the AROME model (Seity et al., 2011) which is centered over France. Lateral boundary conditions are provided by the global model ARPEGE (Action de Recherche Petite Echelle Grande Echelle). As shown in Fig. 8 and still for altitudes from 0.2 to 1.2 km a.m.s.l., the comparison to lidar-derived WVMR for this specific case leads to std of 0.51 and 0.81 g kg^{-1} for ECMWF and AROME-WMED, respectively.

AMTD
6, 10653–10698, 2013

4 ~~Uncertainty sources~~

The different sources of uncertainty playing a major role in both the WVMR and the aerosol optical properties retrievals will be analyzed in this section. For the latter, we will consider the results already published by Chazette et al. (2012b) showing the entire methodology for the same type of lidar.

The uncertainties in the determination of the WVMR are related to 3 main sources: (i) the shot noise characterized by the signal to noise ratio (SNR_λ) of the lidar system, (ii) the calibration related to rawindsoundings, and (iii) the molecular and aerosol contributions. At the first order, the relative error ε_H on r_H is then given by

$$\varepsilon_\mathrm{H} \approx \sqrt{\underbrace{\frac{1}{\mathrm{SNR}_\mathrm{N}^2}+\frac{1}{\mathrm{SNR}_\mathrm{H}^2}}_{\text{Shot noise}}+\underbrace{\varepsilon_K^2+\varepsilon_\xi^2+\varepsilon_\mathrm{HV}^2}_{\text{Calibration}}+\underbrace{\varepsilon_\mathrm{m}^2+\varepsilon_\mathrm{a}^2}_{\text{Atmosphere}}} \quad (13)$$

where ε_K, ε_ξ and ε_HV are the relative errors due to the calibration constant K, the overlap factors and the HV variation, respectively. The relative error associated to the spectral dependency of the extinction properties of molecules (aerosols) is given by $\varepsilon_\mathrm{m}(\varepsilon_\mathrm{a})$.

Shot noise. An accurate assessment of the shot noise contribution requires a precise characterization of the SNR. During nighttime such assessment is easier because the photon counting mode is active. In that mode, the associated standard deviation is the square root of the returned signal (Measures, 1984). An example is given on Fig. 9 for a lidar signal acquired during the night of 19 October 2012 over Menorca with a vertical resolution of 15 m. The SNR is assessed for an average lidar profile over 1000 laser shots. The SNR for a larger number of laser shots p can be easily calculated knowing that it is proportional to $\sqrt{p}$. For a lidar signal averaged over 20 min (20 000 laser shots) and using a Monte Carlo approach as in Royer et al. (2011), the uncertainty on the WVMR has been assessed as close to 0.08 (0.32) g kg^{-1} between 0 and 2 km

AMTD
6, 10653–10698, 2013

(2 and 5 km) a.m.s.l. Figure 10 shows an example obtained during the same day for a representative WVMR vertical profile. Such uncertainties are a little lower than the deviations measured during the inter-comparison between lidar measurements and rawindsoundings.

Calibration. The relative uncertainty on the assessment of the overlap factor F is close to 3 % and comparable to the previous assessment of 5 % performed by Chazette (2003) when using the same approach. This leads to a relative uncertainty $\varepsilon_{\xi} \sim 4$ % for altitudes between 0.3 and 0.80 km a.m.s.l.. The accuracy and precision of the calibration constant K is closely related to the rawindsounding error that is directly linked to the type of radiosonde used for the rawindsounding. It is not easy to obtain such information from meteorological services. Fortunately some papers give the relative uncertainty for some meteorological probes. The rawindsoundings performed over Palma de Majorca used VAISALA RS92 probes. A discussion on various VAISALA probes has been presented in Agusti-Panareda et al. (2009) following the African Monsoon Multidisciplinary Analysis (AMMA) field experiment in 2006 where numerous rawindsoundings were performed. They used the results of the WMO rawindsounding intercomparison experiment (Nash et al., 2005) and the correction used by Ciesielski et al. (2003) for modeling applications. Such a correction has its own uncertainties as explained by Wang et al. (2002, 2008) because it does not take into account the solar heating effect, which affects the measurement during daytime. Moreover, the accuracy is affected by wet and dry biases. The magnitude of the humidity correction is up to 5 % in the lower troposphere but can reach 20 % in the upper troposphere. Ferrare et al. (1995) claim an accuracy of 2–3 % with a precision of 2 %. Such results have been confirmed by Fujiwara et al. (2003) and Bock et al. (2009) for VAISALA RS80 and RS92 probes. Accounting for all these considerations, we consider here that the relative error on the rawindsounding-derived WVMR is about 6 % between 0 and 5 km a.m.s.l.. Associated with the std between the lidar- and rawindsounding-derived WVMR, the calibration error is $\varepsilon_K \sim 6.5$ %. During daytime the effect of the HV variation has to be considered. The uncertainty is here mainly due to the atmospheric fluctuations during

AMTD
6, 10653–10698, 2013

the HV scanning (~ 30 min). For mean lidar profiles of 1000 laser shots (Fig. 6), the additional relative error is high (~ 10 %). During daytime the number of laser shots has to be enhanced (60 000 for 1 h) and this uncertainty should decrease but it is difficult to quantify it. The easiest approach is to compare the lidar-derived WVMR to the one retrieved from daytime rawindsounding as shown in Sect. 3. The calibration error is then around 7 %.

Molecules and aerosols spectral dependencies. The third error source is negligible compared to the others. Indeed, the residual molecular contribution can be easily corrected using a climatologic model as in Chazette et al. (2003) leading to a very low uncertainty, i.e. less than 10^{-3} g kg^{-1} (0.3 g kg^{-1} when not corrected). The presence of aerosol layers leads to an error on r_H close to 0.01 g kg^{-1}. Nevertheless, such a contribution can be accounted for after the retrieval of the AOT derived from N_2-Raman channel.

Synthesis on the WVMR error. Taking into account all the main error sources, the relative VWMR error can be established for 3 different altitude ranges. During nighttime and for a temporal integrated sampling of 20 min (20 000 laser shots), the relative error on the WVMR is ~ 8 % within the first kilometer (0–0.8 km a.m.s.l.). It reaches 11 % between 2 and 5 km a.m.s.l.. The lower relative error is between 0.8 and 2 km a.m.s.l. with a value of ~ 7 %. Of course, the transitions are gradual and these values may change depending on the presence of more or less moist air masses in the middle ~~troposphere. For~~ daytime, the same relative error can be reached in the first kilometer but with 1 h ~~of integration~~. Actually, for ~~operational purpose~~, the error on the WVMR can be calculated for each averaged profile knowing the SNR for both the N_2- and H_2O-channels. The main error source that could be reduced is the one due to the calibration, which is entirely dependent of both the rawindsounding accuracy and precision.

Aerosol optical properties. Uncertainties on the retrieval of aerosol optical properties from similar detection channels ~~are already~~ well discussed in the scientific literature (e.g. Chazette et al., 2010; Royer et al., 2011). For SNR > 20 as encountered with WALI, the relative uncertainty on the LR is ~ 5 % (~ 10 %) during nighttime (daytime).

AMTD
6, 10653–10698, 2013

The relative uncertainty on the VDR and PDR are close to 10 % for the encountered AOT > 0.2. The relative uncertainty on the AOT is less than 2 %.

5 ~~Application to the Mediterranean program~~

WALI was operated during the 2012 fall campaign of the HyMeX program (Special Observing Period 1), between 17 September and 27 October. After the lidar calibration and the assessment of the different error sources, a typical meteorological situation ~~has been studied in terms of both~~ WVMR and aerosols. As shown in Fig. 11, an intense dust aerosol event was observed from 17 to 20 October. The VDR highlights two maxima, one on 18 October and the other on 19 October. This event has been sampled to follow its evolution along time. The different time periods considered are given in Table 2 with the corresponding dust layers and their main optical characteristics. The values of the WVMR are also given ~~and highlight~~ a strong link between dust layers and significant water vapor contents.

Such an application uses the entire capability of the lidar but needs complementary information. Hence, exogenous modeling material has been used. Backtrajectories have been computed to determine ~~airmasses~~ transport routes (Fig. 12) using the NOAA Hybrid Single Particle Lagrangian Integrated Trajectory (HYSPLIT) model (Draxler and Rolph, 2003) with 6 hourly archived meteorological data provided from the US National Centers for Environmental Prediction (NCEP) Global Data Assimilation System (GDAS) at the horizontal resolution of 0.5°. The altitude of the trajectory starting point was selected primarily from the lidar/in-situ observation of aerosol layer height. The WVMR along the airmass trajectory was retrieved by using the HYSPLIT model, which calculates meteorological parameters (i.e., temperature, relative humidity, pressure) along its trajectories. Note that the WVMRs given by the HYSPLIT model were in good agreement with those of balloon-borne data observed at an adjacent rawindsounding site for each time step of the trajectory (Yoon et al., 2006). The outputs

AMTD
6, 10653–10698, 2013

of the ECMWF re-analysis (http://www.ecmwf.int) have also been considered for illustrating the horizontal wind-field.

Before the arrival of the event, winds in the lower troposphere are southwest with low speeds, of the order of 2–5 ms^{-1} (Fig. 13). They are associated with a low-pressure area situated in the South-western part of Ireland. They transport an aerosol layer above the marine boundary layer (MBL) (Fig. 14) from the Spanish coast. In this layer, the mean LR (PDR) is ~ 77 sr (1 %) as it can be expected for this type of pollution particles. The VDR is close to the value of its molecular contribution on the entire sampled atmospheric column (Fig. 14), no desert dust aerosol is present. The higher values of the WVMR are located in the MBL (~ 9–10 gkg^{-1}), whose top altitude remained below 0.5 km a.m.s.l. during all the experiment. A wet layer (> 7 gkg^{-1}) is also present above the MBL where the polluted aerosols are trapped. From the backtrajectories shown in Fig. 12, it appears that this layer might be mainly ~~filled with water vapor~~ off the Balearic Islands. Note that the rawindsounding from Palma de Majorca shows strong similarities with the lidar-derived WVMR profile between the surface and 5 km a.m.s.l. (Fig. 14). It is therefore very likely that the same air mass was sampled above the two sites. Above 2 km a.m.s.l. the free troposphere is reached with a wet layer (WVMR ~ 2–3 gkg^{-1}) between 2 and 3.5 km a.m.s.l.. The aerosol load in this layer is very low and non-depolarizing.

During the night of 17–18 October 2012, the strong prevailing winds veer to the South, bringing relatively warm and humid airmasses from Sahara to Menorca, because of the presence of a cut-off over Ireland, which moves East during the event. Thus, Saharan airmasses penetrate over the Mediterranean from the Algerian coast (Figs. 12 and 13). The Saharan region is the world's major source of natural wind-blown mineral dust aerosol (e.g. Hamonou et al., 1999) and thus aerosol column burden may be enhanced when wind blows from the African coast. Indeed, the AOT (PDR) increases significantly from 0.1 to 0.18 (0.01 to 0.10) whereas the LR decreases to reach ~ 45 sr. Stronger winds (> 10 ms^{-1}) are linked to a stronger WVMR (~ 10 gkg^{-1}) in the lower tropospheric layers. Dust aerosols are present in the MBL but the main dust layer

AMTD
6, 10653–10698, 2013

is between 0.5 and 2.2 km a.m.s.l. associated with $r_H \sim 6\,g\,kg^{-1}$ that contrasts sharply with the content of the free troposphere. Similar observations can be made for the following day. The presence of important amounts of water vapor in the dust aerosol layers, between 4 and $6.7\,g\,kg^{-1}$, may contribute to maintain the particles in well-defined vertical structures along their transport for a longer period of time. The static stability of the layer can thus be enhanced as described by Kim et al. (2007, 2009). In return, dust plumes can act on the high precipitation events that occurred during the experimental period, by leading to the destabilization of the air masses coming from the sea that crossed the regions of Valencia and Tarragona (Spain) and upstream of Lourdes (France), where 24 h accumulated rainfall of ~ 50 mm occurred on 20 October.

The atmospheric transport for 18 and 19 October is presented on Figs. 12, 13 and 15. It confirms what has been described for the morning of 18 October. As the low moved eastward, the wind weakened and the event ended on 20 October (Figs. 12 and 15). The end of the event is associated with intense rainfalls related to the strong humidity of the Saharan airmasses, which underwent subsidence over the Mediterranean Sea, while it caught water above the sea. Thus, the WVMR may have reached more than $15\,g\,kg^{-1}$ at the ground level (Fig. 14). These important amounts of water vapor are to put in parallel with the stronger aerosol extinction coefficients, likely due to the hygroscopic growth of certain particle types. A mix of various aerosol types could be present in the MBL because the PDR remains high in this layer. During all the events, the PDR varied from 0.1 to 0.19 in the aerosol layers (Table 2). Such values are very close to the ones derived by Müller et al. (2007) with the Raman lidar POLIS in the frame of the Saharan Mineral Dust Experiment (SAMUM) with PDR = 0.25 ± 0.08. By cons, the LR marks more significant differences between the aerosol layers. In the MBL, the LR derived from our study is found to be generally higher (~ 70 sr), which is in contrast to what can be expected for marine aerosols with a coarse mode of sea salt whose LR ~ 25 sr (e.g. Flamant et al., 2000). Our derived LR value can be criticized for two reasons. Firstly, the altitude range of the MBL is more sensitive than the upper ones to the assessment of the lidar overlap function. Secondly, the boundary effects of the

AMTD
6, 10653–10698, 2013

regularization method used to retrieve the aerosol optical properties during the night can strongly impact the derivation of the optical properties in the lower layers. Note that higher value of the LR was also retrieved on 17 October when no dust event occurred. Again, the result could be questionable because the AOT is low, close to 0.07, and the inversion procedure could not be well constrained. However, error studies show uncertainty of about 30 % in such cases (e.g. Chazette et al., 2012), which confirms the likely higher values of the LR in the MBL.

For the upper layers that contain ~~likely~~ Saharan dust aerosols only, the LR ranges from 47 to 63 sr. It is significantly variable over the four days sampled. This indicates a high variability of aerosol optical properties and possibly of the particle nature. Different dust sources are activated along the days, as the low moves eastward, resulting in different types of dust particles transported. Moreover, human activities located close to the coast may also explain a part of this variability. The lidar derived LR range can be retrieved from the literature, but little information exists at the wavelength of 355 nm. During the African Monsoon Multidisciplinary Analysis (AMMA), Chazette et al. (2007) found LR between 40 and 67 sr at 355 nm for the Harmattan dust layer above Niamey. During the same project, Kim et al. (2009) analyzed the CALIOP measurements and reported a value of $\overline{LR} \sim 36$–38 sr at 532 nm. Note that the LR generally increases when wavelength decreases. Cattrall et al. (2005) also reported $\overline{LR}$ values close to 43 sr using sunphotometer measurements. Dulac and Chazette (2003) found a $\overline{LR}$ of 59 sr at 532 nm for a multilayer structure with desert, anthropogenic and marine aerosols over the Mediterranean. Moreover, Mattis et al. (2002) used the Raman lidar technique to measure the LR value of elevated dust layers during two episodes over Germany. They report LR values between ~ 50 and 77 sr at 532 nm.

AMTD
6, 10653–10698, 2013

6 Conclusions

Raman lidar systems have been identified by various authors as powerful tools for the atmospheric sampling of both water vapor and aerosols with high vertical resolution (between 15 and 50 m). With the increasing need to study the cycle of these atmospheric components, precise and reliable instruments are highly required. Even if instrumental development of such systems started right after the discovery of the laser effect (Smullin and Fiocco, 1962), recent technology improvements of detectors, optics and electronics, open doors to new scientific and operational capabilities. Hence, the eye-safe transportable Raman lidar WALI has been developed for measuring both the WVMR and the aerosol optical properties in the troposphere. This paper focused on the simultaneous retrieval of the WVMR and aerosol optical properties from the WALI instrument. ~~It insists on the~~ calibration procedure and ~~on the error budget for deriving the WVMR.~~

The original design of the WALI system leads to very good capabilities in terms of low altitude overlap and WVMR retrieval during nighttime, that is to say, with an absolute deviation from rawindsoundings of less than 0.5 g kg^{-1}. The calibration procedure is the main error source for the lidar-derived WVMR, when dealing with a large ~~enough~~ SNR. This error is very dependent on the rawindsounding accuracy and precision. It reaches 11 % in the MBL and decreases to 7 % below 5 km range for a temporal averaging of 20 min and a vertical resolution of 15 m. The precision of measurements can deteriorate very quickly thereafter due to the decreasing SNR with altitude. The determination of the water vapor is more difficult during daytime, but the measurements have been performed with the same uncertainty for altitude ranges below 1 km using a temporal averaging over ~ 1 h.

The uncertainties linked to the retrieval of aerosol optical properties are comparable to the ones of previous Raman mobile lidars developed ~~in the~~ team with a relative error ~~below~~ 10 % for the LR or the PDR retrieval.

AMTD
6, 10653–10698, 2013

To demonstrate its performances for measuring the WVMR and the aerosol optical properties, the WALI system has been implemented in the Menorca Island during fall 2012 in the frame of the Mediterranean projects HyMeX and ChArMEx. It has allowed highlighting a strong event of desert dust aerosols associated with high water vapor contents between the 17 and 20 October 2012. Both the LR and PDR attributed to dust particles are very variable but stay in the range of the variability reported in the literature, between ~ 45–63 ± 6 sr and 0.1–0.19 ± 0.01, respectively. These dust aerosol layers are associated with significant WVMR of ~ 4–$6.7 \pm 0.4\,\mathrm{g\,kg^{-1}}$, which may contribute to the important rain falls observed during this period over the Southwestern Europe.

Acknowledgements. This work was supported by the French Agence Nationale de la Recherche (ANR) via the IODA-MED project, the French space agency (CNES) and the Commissariat à l'Energie Atomique (CEA). We thank D. N. Whiteman for useful information for building the WALI instrument. We also thank M. Sicard for its help for installing the lidar station on the Menorca Island. ECMWF data used in this study have been obtained from the ECMWF Data Server. Meteo-France is gratefully acknowledged for the rawindsounding data and the output of the AROME-WMED model. The authors would additionally like to thank the HyMeX program for the support of this work.

The publication of this article is financed by CNRS-INSU.

References

Agusti-Panareda, A., Vasiljevic, D., Beljaars, A., Bock, O., Guichard, F., Nuret, M., Lafore, J.-P., Andersson, E., Bechtold, P., Fink, A., Hersbach, H., Garcia Mendez, A., Ngamini, J.-B., Parker, D. J., Redelsperger, J. L., and Tompkins, A.: Radiosonde humidity bias correction over the West African region for the special AMMA reanalysis at ECMWF, Q. J. Roy. Meteorol. Soc., 135, 640, 595–617, doi:10.1002/qj.396, 2009.

Ångström, A.: The parameters of atmospheric turbidity, Tellus, 16, 6–75, 1964.

Ansmann, A., Riebesell, M., Wandinger, U., Weitkamp, C., Voss, E., Lahmann, W., and Michaelis, W.: Combined raman elastic-backscatter LIDAR for vertical profiling of moisture, aerosol extinction, backscatter, and LIDAR ratio, Appl. Phys. B, 55, 18, 1992.

Bock, O. and Nuret, M.: Verification of NWP model analyses and radiosonde humidity data with GPS precipitable water vapor estimates during AMMA, Weather Forecast., 24, 1085–1101, doi:10.1175/2009WAF2222239.1, 2009.

Boucher, O. and Anderson, L.: General circulation model assessment of the sensitivity of direct climate forcing by anthropogenic sulfate aerosols to aerosol size and chemistry, J. Geophys. Res., 100, 26117–26134, 1995.

Bribes, J. L., Gaufres, R., Monan, M., Lapp, M., and Penney, C. M.: Raman band contours for water vapor as a function of temperature, Appl. Phys. Lett., 28, 336–337, 1976.

Bruneau, D., Quaglia, P., Flamant, C., Meissonnier, M., and Pelon, J.: Airborne Lidar LEANDRE II for water-vapor profiling in the Troposphere. I. System description, Appl. Optics, 40, 3450–3461, 2001.

Cattrall, C., Reagan, J., Thome, K., and Dubovik, O.: Variability of aerosol and spectral lidar and backscatter and extinction ratios of key aerosol types derived from selected Aerosol Robotic Network locations, J. Geophys. Res., 110, D10S11, doi:10.1029/2004JD005124, 2005.

Ciesielski, P. E., Johnson, R. H., Haertel, P. T., and Wang, J.: Corrected TOGA COARE sounding humidity data: impact on diagnosed properties of convection and climate over the warm pool, J. Climate, 16, 2370–2384, 2003.

Chazette, P.: The monsoon aerosol extinction properties at Goa during INDOEX as measured with lidar, J. Geophys. Res., 108, 4187, doi:10.1029/2002JD002074, 2003.

Chazette, P., Couvert, P., Randriamiarisoa, H., Sanak, J., Bonsang, B., Moral, P., Berthier, S., Salanave, S., and Toussaint, F.: Three dimensional survey of pollution during winter in French Alps valleys, Atmos. Environ., 39, 1345–1047, 2005.

AMTD
6, 10653–10698, 2013

Chazette, P., Sanak, J., and Dulac, F.: New approach for aerosol profiling with a lidar onboard an ultralight aircraft: application to the African Monsoon Multidisciplinary Analysis, Environ. Sci. Technol., 41, 8335–8341, 2007.

Chazette, P., Raut, J.-C., Dulac, F., Berthier, S., Kim, S.-W., Royer, P., Sanak, J., Loaëc, S., and Grigaut-Desbrosses, H.: Simultaneous observations of lower tropospheric continental aerosols with a ground-based, an airborne, and the spaceborne CALIOP lidar systems, J. Geophys. Res., 115, D00H31, doi:10.1029/2009JD012341, 2010.

Chazette, P., Dabas, A., Sanak, J., Lardier, M., and Royer, P.: French airborne lidar measurements for Eyjafjallajökull ash plume survey, Atmos. Chem. Phys., 12, 7059–7072, doi:10.5194/acp-12-7059-2012, 2012a.

Chazette, P., Bocquet, M., Royer, P., Winiarek, V., Raut, J.-C., Labazuy, P., Gouhier, M., Lardier, M., and Cariou, J.-P.: Eyjafjallajökull ash concentrations derived from both lidar and modeling, J. Geophys. Res., 117, D00U14, doi:10.1029/2011JD015755, 2012b.

Collis, R. T. H. and Russell, P. B.: Lidar measurement of particles and gases by elastic backscattering and differential absorption, in: Laser Monitoring of the Atmosphere, edited by: Hinkley, E. D., Springler-Verlag, New York, 71–152, 1976.

Cooney, J. A.: Remote measurements of atmospheric water vapor profiles using the Raman component of laser backscatter, J. Appl. Meteorol., 9, 182–184, 1970.

Draxler, R. R. and Rolph, G. D.: HYSPLIT (HYbrid Single-Particle Lagrangian Integrated Trajectory) Model access via NOAA ARL READY Website, available at: http://www.arl.noaa.gov/ready/hysplit4.html (last access: 8 December 2013), NOAA Air Resources Laboratory, Silver Spring, MD, 2003.

Dulac, F. and Chazette, P.: Airborne study of a multi-layer aerosol structure in the eastern Mediterranean observed with the airborne polarized lidar ALEX during a STAAARTE campaign (7 June 1997), Atmos. Chem. Phys., 3, 1817–1831, doi:10.5194/acp-3-1817-2003, 2003.

Fiocco, G. and Grams, G.: Observations of the aerosol layer at 20 km by optical radar, J. Atmos. Sci., 21, 323–324, 1964.

Fiocco, G. and Smullin, L. D.: Detection of scattering layers in the upper atmosphere (60–140 km) by optical radar, Nature, 199, 1275–1276, doi:10.1038/1991275a0, 1963.

Flamant, C., Pelon, J., Chazette, P., Trouillet, V., Quinn, P., Frouin, R., Bruneau, D., Léon, J. F., Bates, T., Johnson, J., and Livingston, J.: Airborne lidar measurements of aerosol spatial

AMTD
6, 10653–10698, 2013

distribution and optical properties over the Atlantic Ocean during an European pollution outbreak of ACE-2, Tellus B, 52, 662–667, 2000.
Fujiwara, M., Shiotani, M., Hasebe, F., Vömel, H., Oltmans, S. J., Ruppert, P. W., Horinouchi, T., and Tsuda, T.: Performance of the Meteolabor "Snow White" chilled-mirror hygrometer in the tropical troposphere: comparisons with the Vaisala RS80 A/H-humicap sensors, J. Atmos. Ocean. Tech., 20, 1534–1542, 2003.
Giorgi, F. and Lionello, P.: Climate change projections for the Mediterranean region, Global Planet. Change, 63, 90–104, 2008.
Hamonou, E., Chazette, P., Balis, D., Dulac, F., Schneider, X., Galani, E., Ancellet, G., and Papayannis, A.: Characterisation of the vertical structure of Saharan dust export to the Mediterranean Basin, J. Geophys. Res., 18, 2257–2270, 1999.
Haywood, J. M., Roberts, D. L., Slingo, A., Edwards, J. M., and Shine, K. P.: General circulation model calculations of the direct radiative forcing by anthropogenic sulphate and fossil-fuel soot aerosol, J. Climate, 10, 1562, doi:10.1175/1520-0442(1997)010<1562:GCMCOT>2.0.CO;2, 1997.
Higdon, N. S., Browell, E. V., Ponsardin, P., Grossmann, B. E., Butler, C. F., Chyba, T. H., Mayo, M. N., Allen, R. J., Heuser, A. W., Grant, W. B., Ismail, S., Mayor, S. D., and Carter, A. F.: Airborne differential absorption lidar system for measurements of atmospheric water vapor and aerosols, Appl. Optics, 33, 6422–6438, 1994.
Kim, S.-W., Yoon, S.-C., Jefferson, A., Won, J.-G., Dutton, E. G., Ogren, J. A., and Anderson, T. L.: Observation of enhanced water vapor in Asian dust layer and its effect on atmospheric radiative heating rates, Geophys. Res. Lett., 31, L18113, doi:10.1029/2004GL020024, 2004.
Kim, S.-W., Chazette, P., Dulac, F., Sanak, J., Johnson, B., and Yoon, S.-C.: Vertical structure of aerosols and water vapor over West Africa during the African monsoon dry season, Atmos. Chem. Phys., 9, 8017–8038, doi:10.5194/acp-9-8017-2009, 2009.
King, L. V.: On the complex anisotropic molecule in relation to the dispersion and scattering of light, P. R. Soc. Lond. Series 1, 104, 333–357, 1923.
Klett, J. D.: Lidar inversion with variable backscatter/extinction ratios, Appl. Optics, 24, 1638–1643, 1985.
Kulmala, M., Laaksonen, A., Korhonen, P., Vesala, T., and Ahonen, T.: The effect of atmospheric nitric acid vapor on cloud condensation nucleus activation, J. Geophys. Res., 98, D12, 22949–22958, 1993.

AMTD
6, 10653–10698, 2013

Larson, T. V. and Taylor, G. S.: On the evaporation of NH_4NO_3 aerosol, Atmos. Environ., 17, 2489–2595, 1983.
Mattis, I., Ansmann, A., Müller, D., Wandinger, U., and Althausen, D.: Dual-wavelength Raman lidar observations of the extinction-to-backscatter ratio of Saharan dust, Geophys. Res. Lett., 29, 20.1–20.4, doi:10.1029/2002GL014721, 2002.
Mattis, I., Siefert, P., Müller, D., Tesche, M., Hiebsch, A., Kanitz, T., Schmidt, J., Finger, F., Wandinger, U., and Ansmann, A.: Volcanic aerosol layers observed with multiwavelength Raman lidar over central Europe in 2008–2009, J. Geophys. Res., 115, D00L04, doi:10.1029/2009JD013472, 2010.
Measures, R. M.: Laser Remote Sensing: Fundamentals and Applications, Wiley & Sons, NewYork, 1984.
Melfi, S. H., Lawrence Jr., J. D., and McCormic, M. P.: Observation of Raman scattering by water vapor in the atmosphere, Appl. Phys. Lett., 15, 295–297, 1969.
Melfi, S. H., Whiteman, D. N., and Ferrare, R.: Observation of atmospheric fronts using Raman lidar moisture measurements, J. Appl. Meteorol., 28, 789–806, 1989.
Müller, D., Ansmann, A., Mattis, I., Tesche, M., Wandinger, U., Althausen, D., and Pisani, G.: Aerosol-type-dependent lidar-ratio observed with Raman lidar, J. Geophys. Res., 112, D16202, doi:10.1029/2006JD008292, 2007.
Nash, J., Smout, R., Oakley, T., Pathnack, B., and Kumosenko, S.: WMO Intercomparison of High Quality Radiosonde Systems, Vacoas, Mauritius, 2–25 February 2005, WMO report, February 2005, available at: http://www.wmo.int/pages/prog/www/ (last access: 8 December 2013), 2005.
Nicolet, M.: On the molecular scattering in the terrestrial atmosphere, Planet. Space Sci., 32, 1467–1468, doi:10.1016/0032-0633(84)90089-8, 1984.
Penney, C. M. and Lapp, M.: Raman-scattering cross sections for water vapor, J. Opt. Soc. Am., 66, 422–425, 1976.
Raut, J.-C. and Chazette, P.: Assessment of vertically-resolved PM_{10} from mobile lidar observations, Atmos. Chem. Phys., 9, 8617–8638, doi:10.5194/acp-9-8617-2009, 2009.
Rood, M. J., Covert, D. S., and Larson, T. V.: Hygroscopic properties of atmospheric aerosol in Riverside, California, Tellus B, 39, 383–397, 1987.
Royer, P., Chazette, P., Lardier, M., and Sauvage, L.: Aerosol content survey by mini-N2-Raman lidar: application to local and long-range transport aerosols, Atmos. Environ., 45, 7487–7495,, doi:10.1016/j.atmosenv.2010.11.001, 2011.

AMTD
6, 10653–10698, 2013

Sanchez-Gomez, E., Somot, S., and Mariotti, A.: Future changes in the Mediterranean water budget projected by an ensemble of regional climate models, Geophys. Res. Lett., 36, L21401, doi:10.1029/2009GL040120, 2009.
Seity, Y., Brousseau, P., Malardel, S., Hello, G., Benard, P., Bouttier, F., Lac, C., and Masson, V.: The AROME-France convective-scale operational model, Mon. Weather Rev., 139, 976–991, doi:10.1175/2010MWR3425.1, 2011.
Tikhonov, A. E. and Arsenin, V. Y.: Solutions of Ill-Posed Problems, Wiley, 1977.
Turner, D. D. and Goldsmith, J. E. M.: Twenty-Four-Hour Raman Lidar Water Vapor Measurements during the Atmospheric Radiation Measurement Program's 1996 and 1997 Water Vapor Intensive Observation Periods, J. Atmos. Ocean. Tech., 16, 1062–1076, 1999.
Vaughan, G., Wareing, D. P., Thomas, L., and Mitev, V.: Humidity measurements in the free troposphere using Raman backscatter, Q. J. Roy. Meteorol. Soc., 114, 1471–1484, 1988.
Veselovskii, I. A., Cha, H. K., Kim, D. H., Choi, S. C., and Lee, J. M.: Raman lidar for the study of liquid water and water vapor in the troposphere, Appl. Phys. B, 71, 113–117, doi:10.1007/s003400000290, 2000.
Wang, J. and Zhang, L.: Systematic errors in global radiosonde precipitable water data from comparison with ground-based GPS measurements, J. Climate, 21, 2218–2238, 2008.
Wang, J., Cole, H. L., Carlson, D. J., Miller, E. R., and Beierle, K.: Corrections of humidity measurement error from the Vaisala RS80 radiosonde – application to TOGA COARE data, J. Atmos. Ocean. Techn., 19, 981–1002, 2002.
Whiteman, D. N., Melfi, S. H., and Ferrare, R. A.: Raman lidar system for the measurement of water vapor and aerosols in the Earth's atmosphere, Appl. Optics, 31, 3068–3082, 1992.
Whiteman, D. N., Rush, K., Veselovskii, I., Cadirola, M., Comer, J., Potter, J. R., and Tola, R.: Demonstration measurements of water vapor, cirrus clouds, and carbon dioxide using a high-performance Raman lidar, J. Atmos. Ocean. Tech., 24, 1377–1388, 2007.
Yoon, S.-C., Kim, S.-W., Kim, J., Sohn, B.-J., Jefferson, A., Choi, S.-J., Cha, D.-H., Lee, D.-K., Anderson, T. L., Doherty, S. J., and Weber, R. J.: Enhanced water vapor in asian dust layer: entrainment processes and implication for aerosol optical properties, Atmos. Environ., 40, 2409–2421, 2006.

AMTD
6, 10653–10698, 2013

Table 1. Main technical characteristics of the WALI instrument.

Laser	Nd:Yag
Energy	60 mJ at 355 nm
Frequency	20 Hz
Reception channels	Elastic total 354.67 nm
	Elastic ⊥354.67 nm
	Raman-N_2 386.63 nm
	Raman-H_2O 407.5 nm
Reception diameters	15 cm
Field of view	~ 2.3 mrad
Full overlap	~ 300 m
Detector	Photomultiplier tubes
Filter bandwidths	0.2–0.3 nm
Vertical sampling	0.75 m (analog)
	15 m (photon counting)
Vertical resolution	~ 30 m
Acquisition system	PXI technology at 200 MHz

AMTD
6, 10653–10698, 2013

Table 2. Analysis of the dust event of 17 to 20 October over Menorca: different dust layers and their LIDAR derived WVMR and aerosol optical properties for 7 different time periods. The main dust layers are highlighted in bold.

Date	Altitude range (km)	AOT at 355 nm (0.25 to 5 km)		$\overline{r_H}$ ($g\,kg^{-1}$)	$\overline{LR}$ (sr)		$\overline{PDR}$
17 00:00–03:00 LT	0.3–1.0	~ 0.07	0.04	8.8 ± 0.6	74	67 ± 8	0.01± < 0.01
	2–3.5		< 0.01	2.8 ± 0.3		–	–
18 00:00–03:00 LT	0.3–0.5	~ 0.17	0.03	10.0 ± 3	45	66 ± 3	0.1 ± 0.01
	0.5–2.0		0.09	6.4 ± 0.4		47 ± 6	0.1 ± 0.01
18 10:30–14:30 LT	0.3–1	~ 0.38	0.06	7.9 ± 2	59	–	0.15 ± 0.02
	1.5–3		**0.21**	–		–	**0.16 ± 0.01**
18 21:00–24:00 LT	0.5–1.5	~ 0.29	0.09	5.8 ± 0.4	71	69 ± 7	0.16 ± 0.01
	1.5–4		**0.12**	**4.1 ± 0.4**		**63 ± 2**	**0.19 ± 0.01**
19 00:00–03:00 LT	0.5–1.5	~ 0.38	0.09	6.3 ± 0.8	63	58 ± 8	0.12 ± 0.01
	2–3.5		**0.12**	**4.0 ± 0.2**		**53 ± 2**	**0.18 ± 0.01**
19 03:00–06:00 LT	0.3–1.0	~ 0.46	0.07	7.2 ± 2	60	69 ± 15	0.15 ± 0.02
	1.0–3.5		**0.32**	**4.7 ± 1**		**60 ± 4**	**0.18 ± 0.01**
20 00:00–03:00 LT	0.5–1.0	~ 0.14	0.03	7.6 ± 0.2	53	59 ± 7	0.10 ± 0.01
	1.0–2.5		0.07	6.7 ± 0.5		40 ± 2	0.10 ± 0.01

AMTD
6, 10653–10698, 2013

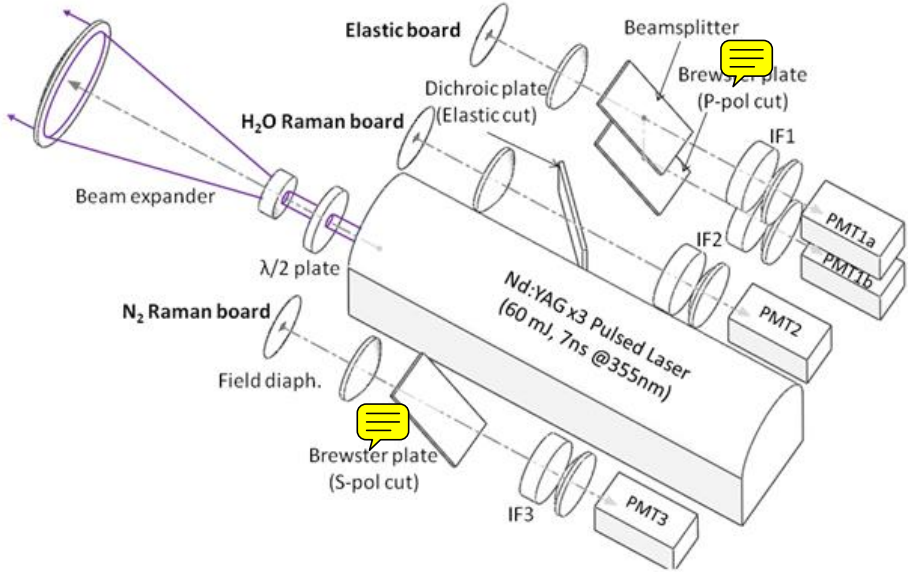

Fig. 1. Schematic representation of the WALI. The receiver refractive telescopes, located on each path before the field diaphragm, were omitted for clarity. The 3 separate detection boards are highlighted with their main components. The emission size is adapted using a beam expander to fulfill eye-safe conditions. The elastic (354.67 nm) detection board is composed of 2 polarization channels: total and cross-polarized. The separation of the radiation over the 2 channels is done using a beam-splitter plate. The N_2-Raman detection board (386.63 nm) is equipped with a 386.63 nm working-wavelength Brewster plate to get rid of half of the sky-background. The H_2O-channel detection board (407.5 nm) is equipped with an additional dichroic plate to ensure a total rejection of the fundamental radiation at 354.67 nm.

AMTD
6, 10653–10698, 2013

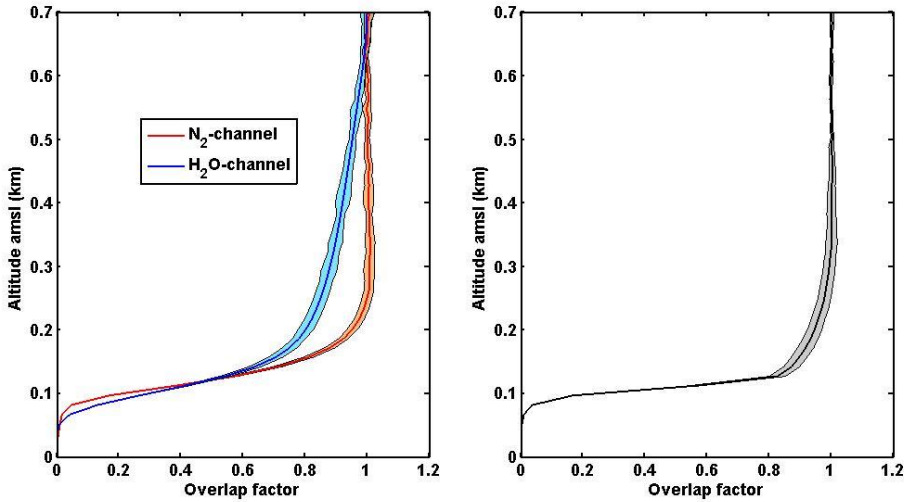

Fig. 2. WALI Overlap factors for the N_2-, H_2O-channels (left) and elastic channel (right) as experimentally measured. The colored areas represent the standard deviations of the overlap factors.

AMTD
6, 10653–10698, 2013

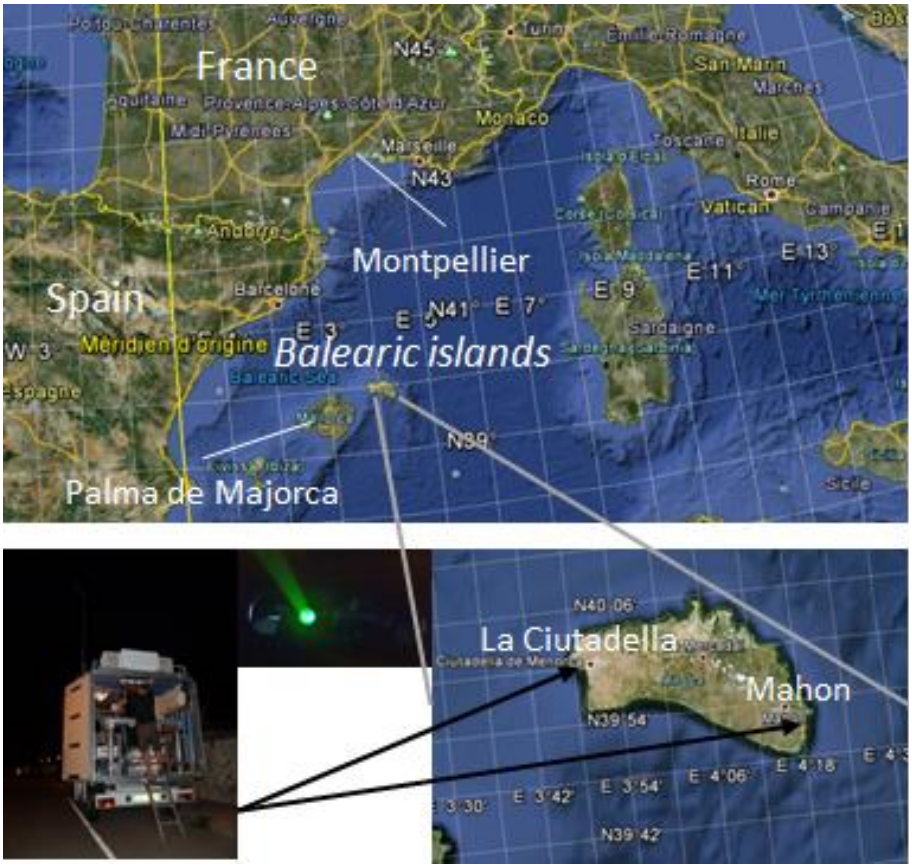

Fig. 3. Southern experimental sites selected for both the HyMeX/IODA-MED and the ChArMEx campaigns. The ground-based lidar-van is shown on the bottom-left. The main experimental sites are indicated on the map (courtesy of Google Inc.).

AMTD
6, 10653–10698, 2013

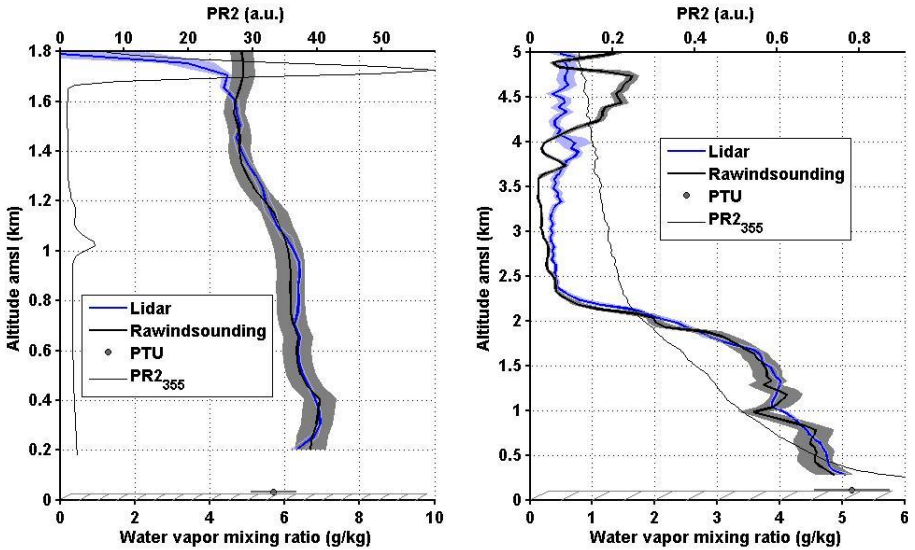

Fig. 4. WALI WVMR retrieval calibration by comparison to rawindsounding: in Montpellier on 30 October 2012 22:00 LT (left) and in Palaiseau (Paris area) on 1 September 2012 01:00 LT (right). PTU stands for the ground-based measurements at ~ 10 m from the surface. The gray areas represent the uncertainties of the rawindsounding.

AMTD
6, 10653–10698, 2013

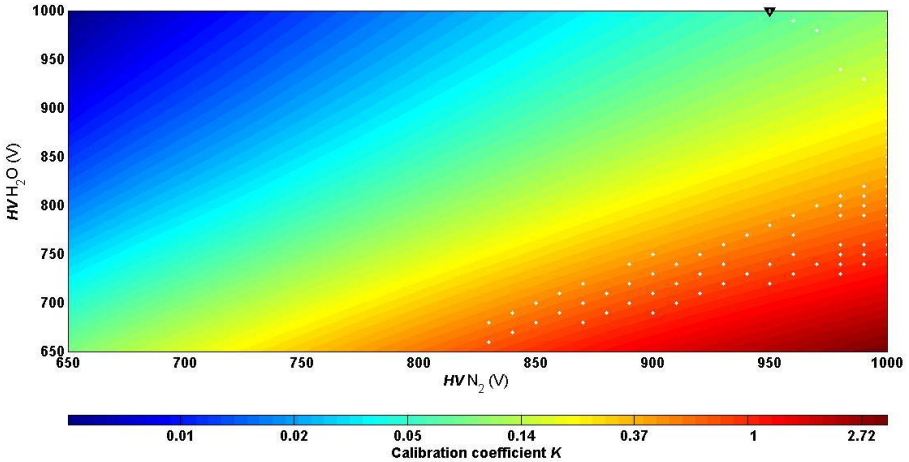

Fig. 5. Photomultiplier High Voltage (HV) dependent calibration coefficient K with respect to N_2 channel and H_2O channel HVs. The black triangle locates the usual night-time setup. The white dots represent the automatic selected HVs during daytime.

AMTD
6, 10653–10698, 2013

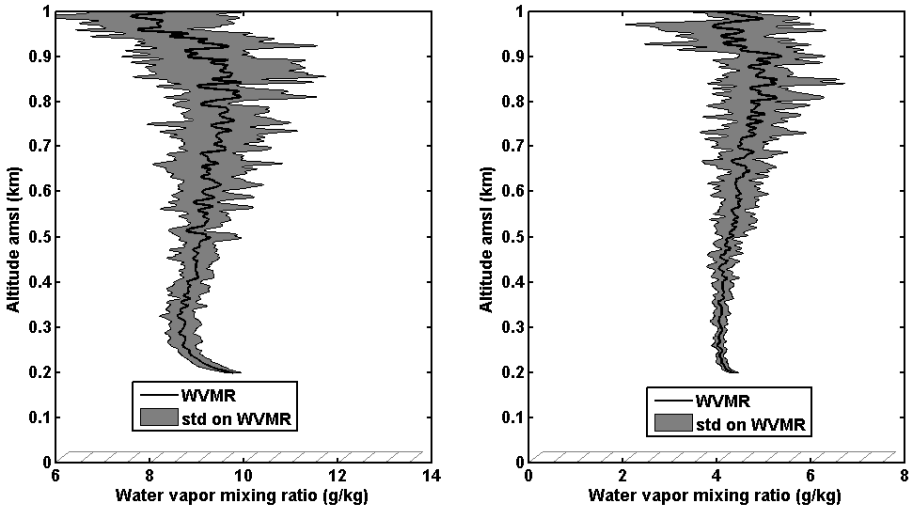

Fig. 6. Test of the WVMR calibration for HVs varying between 650 and 1000 V over the Menorca site (on 21 October 2012 from 20:00 to 20:30 LT) (left) and the Paris area (8 November 2012 from 17:45 to 18:15 LT). Both the mean value and the standard deviation (gray area) computed on the WVMR retrieval are derived from lidar profiles associated with the different HVs.

AMTD
6, 10653–10698, 2013

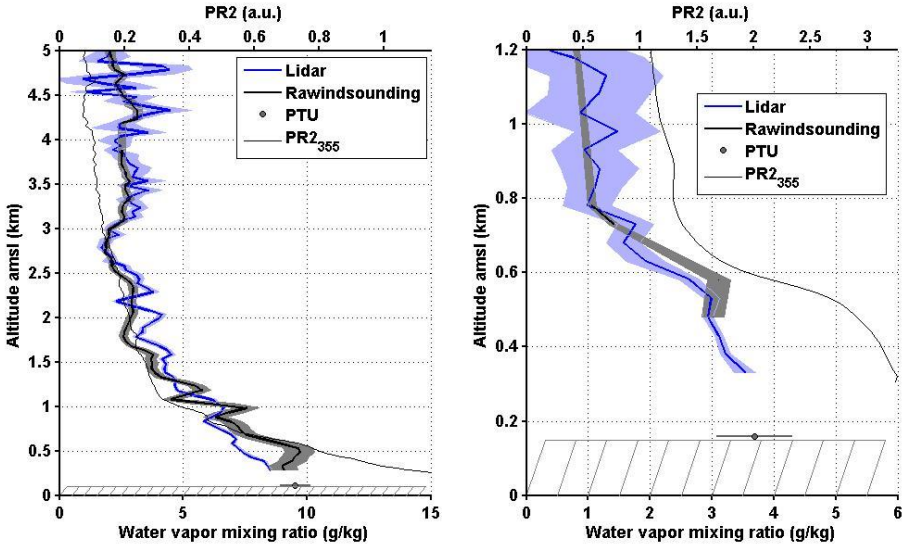

Fig. 7. Calibration validation by comparing lidar derived WVMR to rawindsounding in Paris area before IODA-MED experiment on 5 September 2012 00:50–01:15 LT (left) and after IODA-MED on 19 February 2013 12:30–13:00 LT (right). The gray (blue) areas give the standard deviations around the VWMR mean value derived from the rawindsoundings (lidar). PTU stands for the ground-based measurements at ~ 10 m from the surface.

AMTD
6, 10653–10698, 2013

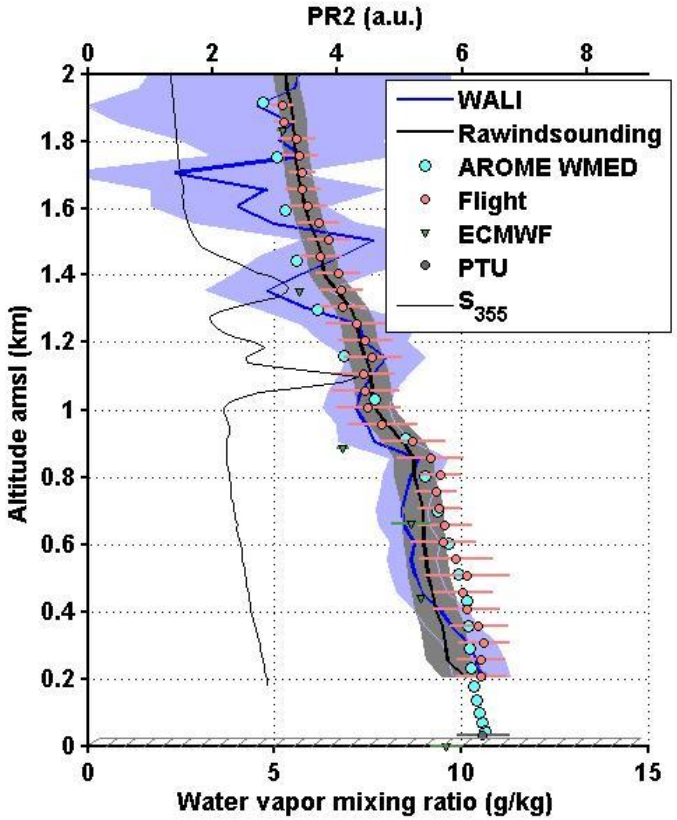

Fig. 8. Comparison of lidar-derived WVMR in Ciutadella to airborne in-situ measurements during a flight over Mahon, Palma rawindsounding and ECMWF and AROME-WMED model outputs on 27 October 2012 08:30 to 09:30 LT. The gray (blue) areas give the standard deviations around the WVMR mean value derived from the rawindsoundings (lidar). PTU stands for the ground-based measurements at ~ 10 m from the surface.

AMTD
6, 10653–10698, 2013

The mobile Water vapor Aerosol Raman LIdar

P. Chazette et al.

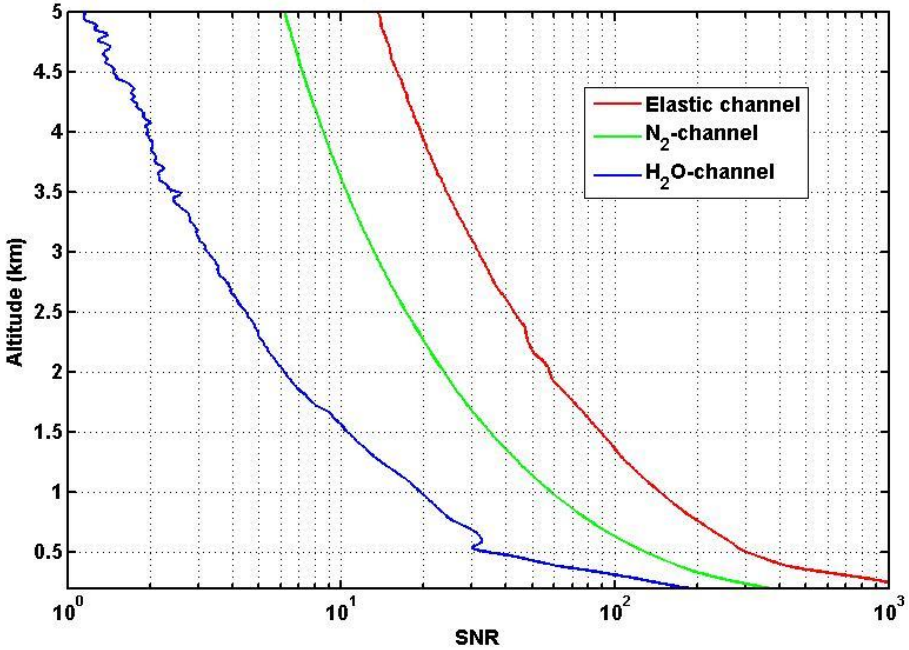

Fig. 9. WALI Signal to Noise Ratio (SNR) as a function of altitude for 3 channels (Elastic, N_2-Raman and H_2O-Raman) for a 1000 shots average lidar profile obtained on 19 October 2012 during nighttime over Menorca.

AMTD
6, 10653–10698, 2013

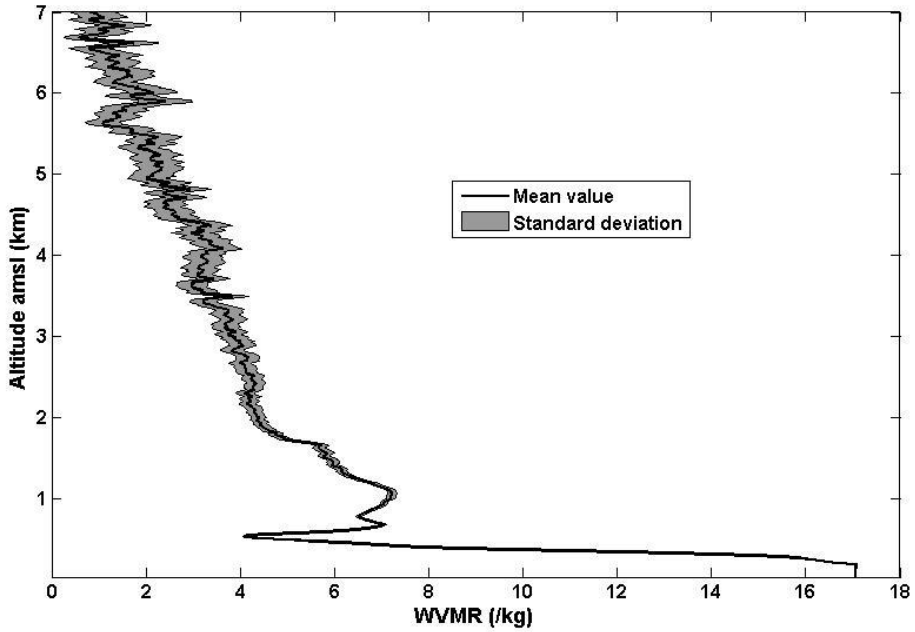

Fig. 10. WALI derived-WVMR profile (black) and its associated standard deviation (gray) averaged over 20 min (20000 laser shots) during the night of 19 October 2012 over Menorca.

AMTD
6, 10653–10698, 2013

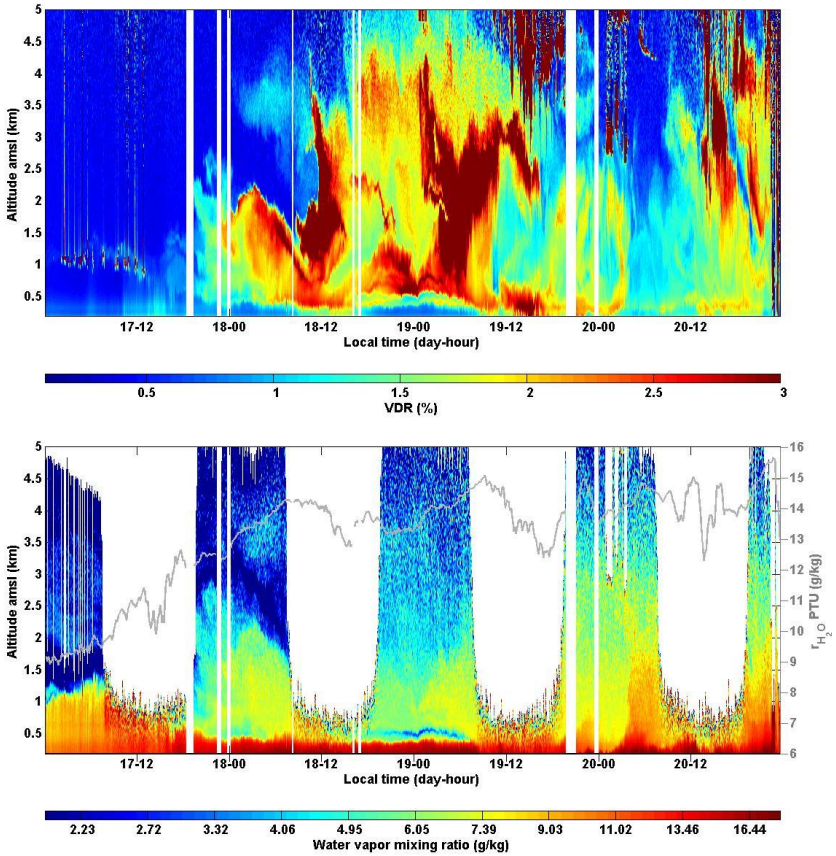

Fig. 11. WALI lidar derived VDR (up) and WVMR (down) from 17 October to 20 October over Menorca. The gray solid line represents ground-based WVMR measurements from a meteorological probe at ~ 10 m from the surface.

AMTD
6, 10653–10698, 2013

The mobile Water vapor Aerosol Raman LIdar

P. Chazette et al.

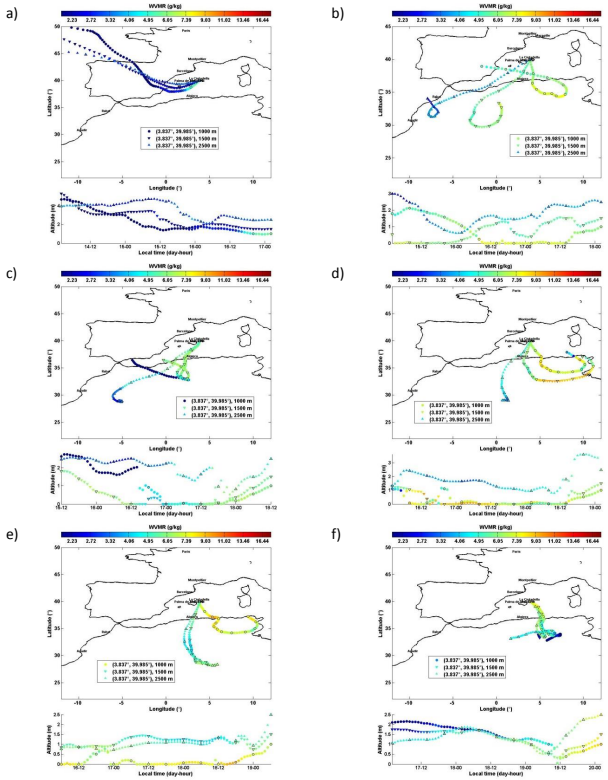

Fig. 12. Backtrajectories between the 17 and 20 October 2012. They have been computed using the Hysplit model (courtesy of NOAA Air Resources Laboratory; http://www.arl.noaa.gov). The wind fields are from GDAS (Global Data Assimilation System, http://www.ncep.noaa.gov/) at the horizontal resolution of 0.5°. The terminal location of the air masses is the site of Ciutadella for the altitudes: 1, 1.5 and 2.5 km a.m.s.l. The color bar represents the WVMR along the trajectories.

AMTD
6, 10653–10698, 2013

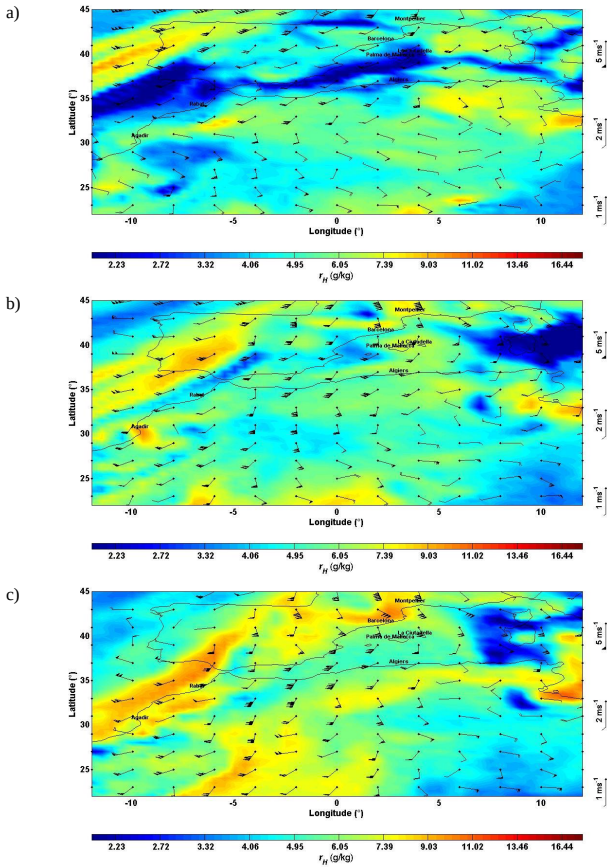

Fig. 13. Wind-field (wind barbs) and WVMR (r_H) (color plot) from ECMWF OPERA 0.5° horizontal resolution analysis at 850 hPa level for 17 October at 02:00 LT **(a)**, 18 October 02:00 LT **(b)**, and 18 October 14:00 LT **(c)**.

AMTD
6, 10653–10698, 2013

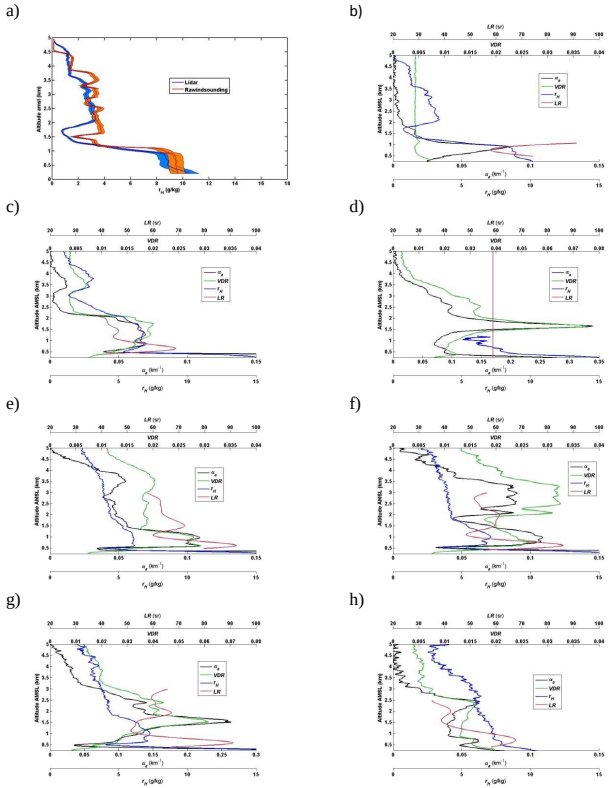

Fig. 14. Comparison between lidar derived WVMR (r_H) and rawindsounding on 17 October 00:00–03:00 LT **(a)**, and WALI derived parameters: extinction coefficient (α_a), VDR, WVMR (r_H) and LR for sampled times of Table 2, i.e. 17 October 00:00–03:00 LT **(b)**, 18 October 00:00–03:00 LT **(c)**, 18 October 10:30–14:30 LT **(d)**, 18 October 21:00–00:00 LT **(e)**, 19 October 00:00–03:00 LT **(f)**, 19 October 03:00–06:00 LT **(g)**, 20 October 00:00–03:00 LT **(h)**.

AMTD
6, 10653–10698, 2013

The mobile Water vapor Aerosol Raman LIdar

P. Chazette et al.

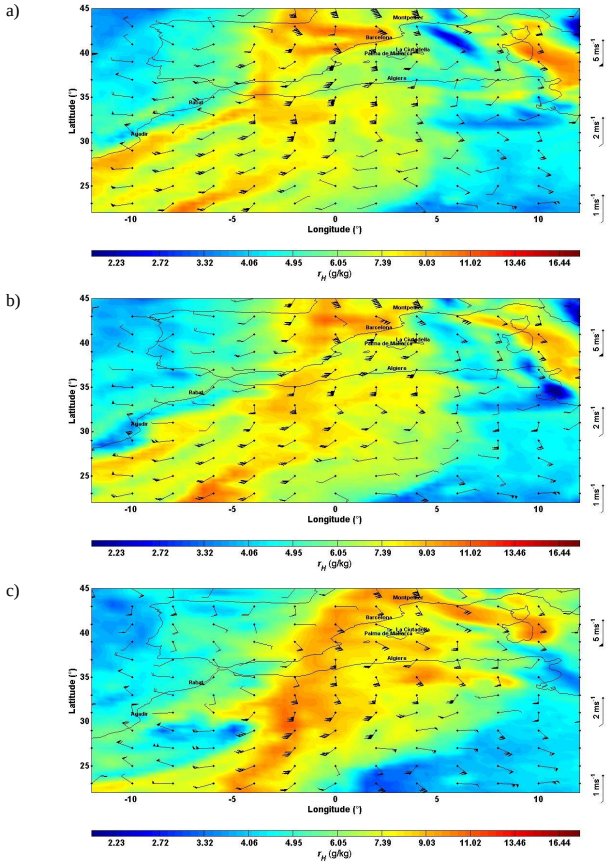

Fig. 15. Wind-field (wind barbs) and WVMR (r_H) (color plot) from ECMWF OPERA 0.5° horizontal resolution analysis at 850 hPa level for 19 October at 02:00 LT **(a)**, 19 October 08:00 LT **(b)**, and 20 October 02:00 LT **(c)**.

AMTD
6, 10653–10698, 2013